A high order approximation of hyperbolic conservation laws in networks:
application to one-dimensional blood flow

Lucas O. Müller[a,*], Pablo J. Blanco[a]

a *Computer Science Department, National Laboratory for Scientific Computing, LNCC/MCTI,*
Av. Getúlio Vargas 333, 25651-075, Petrópolis, RJ, Brazil
INCT-MACC, Institute of Science and Technology in Medicine Assisted by Scientific Computing, Petrópolis, Brazil

Abstract

We present a methodology for the high order approximation of hyperbolic conservation laws in networks by using the Dumbser-Enaux-Toro solver and exact solvers for the *classical* Riemann problem at junctions. The proposed strategy can be applied to any hyperbolic system, conservative or non-conservative, and possibly with flux functions containing discontinuous parameters, as long as an exact or approximate Riemann problem solver is available. The methodology is implemented for a one-dimensional blood flow model that considers discontinuous variations of mechanical and geometrical properties of vessels. The achievement of formal order of accuracy, as well as the robustness of the resulting numerical scheme, are verified through the simulation of both, academic tests and physiological flows.

Keywords:
High order schemes, fully explicit methods, finite volume schemes, junctions.

1. Introduction

We are concerned with hyperbolic conservation laws for which relevant applications include the treatment of networks consisting of one-dimensional domains, hereafter referred to as *edges*, sharing their boundaries, hereafter referred to as *vertexes*. Relevant applications regard traffic flow [1], gas flow in pipes [2, 3], open channel flows and water distribution networks [4, 5, 6] and the modelling of the circulatory system [7, 8, 9, 10, 11]. A crucial aspect for this kind of applications is how to provide boundary conditions at terminal vertexes and algebraic coupling conditions between one-dimensional domains at internal vertexes. A common practice for choosing the coupling conditions is to identify a problem specific quantity, as could be the pressure in the case of isentropic Euler equations [12], or the total pressure in the case of blood flow [13]. Then, the numerical scheme is adapted in order to consistently enforce the devised coupling condition.

In the case of explicit schemes that make use of numerical fluxes at computational cell interfaces, such as finite volume or discontinuous Galerkin schemes, there exists a formal approach that can be pursued. In practice, defining the coupling conditions at an internal vertex P, shared by N_P edges, can be seen as the resolution of a *classical* Riemann Problem (RP) for a junction of N_P one-dimensional domains. This problem was deeply discussed in [6], for example. Under the

---

*Corresponding author
Email address: `lmuller@lncc.br` (Lucas O. Müller)

assumption of sub-sonic flow, the hyperbolic system will provide the necessary wave relations to link the states provided by one-dimensional domains sharing a vertex, as in the case of the classic Riemann problem [14]. Therefore, in order to obtain coupling conditions that are completely consistent with the underlying hyperbolic conservation law, the Riemann problem at the junction has to be solved and the resulting Godunov state can then be used to compute numerical fluxes needed by the explicit scheme to evolve the solution within the one-dimensional domain.

In the case of explicit high order finite volume schemes, one has non-constant data as initial conditions for the Riemann problem at the junction. This specific Cauchy problem is known as the Generalized Riemann Problem (GRP) [15]. In the case of an internal vertex, it is essential to adopt a numerical methodology that solves the GRP at this location accurately enough in order to preserve the formal accuracy of the scheme used for the resolution of conservation laws within the one-dimensional domain. To the best of our knowledge, the first work presenting a methodology to achieve arbitrary high order accuracy in this context was proposed in [16], where the authors used a particular version of a class of numerical schemes known as ADER schemes [17], allowing for arbitrary high order accuracy via one-step numerical methods.

Here, always within the ADER framework, we adopt a different methodology, the Dumbser-Enaux-Toro Riemann solver [18] and adapt certain ingredients to the specificity of the problem under study. This GRP solver requires a high order spatial reconstruction, which in this work is performed using the WENO procedure [19, 20] and a classical RP solver. Special attention must be placed in the choice of the classical RP solver, since in this kind of applications parameters present in the flux function might be discontinuous and the RP solver should be able to deal with this characteristic of the problem in an appropriate manner.

The proposed methodology allows for arbitrarily accurate approximations of hyperbolic conservation laws in networks. In order to illustrate and validate the methodology, we implement the high order treatment of coupling conditions for a one-dimensional blood flow model, using the exact classical RP solver proposed in [21]. This mathematical model incorporates several specific features, such as the treatment of discontinuous parameters in the flux function and the propagation of shocks (or elastic jumps). These features can be found in other applications, such as gas flow in pipes with varying cross-sectional area [22] or open channel flow with variable topography [23].

The rest of the paper is structured as follows. In Section 2 we introduce the mathematical model chosen to illustrate the proposed methodology, which is then developed. Next, in Section 3 we perform a series of tests to verify the accuracy and robustness of the proposed methodology. First we verify that the expected order of accuracy is achieved by solving a test with exact solution. Then we solve a series of test problems on simple networks, including smooth and discontinuous solutions. We conclude the tests by solving the one-dimensional equations on an arterial network model with appropriate boundary conditions. Final remarks are drawn in Section 4.

2. Methods

In this section we present the mathematical model adopted to illustrate the proposed methodology. Then we show how to solve the *classical* RP at an internal vertex. Finally, we propose how to accurately solve the GRP at this location.

2.1. One-dimensional blood flow model with variable vessel properties

One-dimensional blood flow in deformable vessels is described by the following hyperbolic system

$$\begin{cases} \partial_t A + \partial_x q = 0\,, \\[2mm] \partial_t q + \partial_x \left(\dfrac{q^2}{A} \right) + \dfrac{A}{\rho}\partial_x p = -\dfrac{f}{\rho}\,, \end{cases} \tag{1}$$

where x is the axial coordinate along the longitudinal axis of the vessel; t is time; $A(x,t)$ is the cross-sectional area of the vessel; $q(x,t)$ is the flow rate; $p(x,t)$ is the average internal pressure over a cross-section; $f(x,t) = \gamma\pi\mu\frac{q}{A}$ is the friction force per unit length of the tube, with γ depending on the velocity profile; μ is the fluid viscosity and ρ is the fluid density.

Pressure $p(x,t)$ is related to the cross-sectional area $A(x,t)$ by the algebraic relation of the form

$$p(x,t) = K(x)\phi(A(x,t),A_0(x)) + p_e(x,t) = K(x)\left[\left(\frac{A(x,t)}{A_0(x)} \right)^m - \left(\frac{A(x,t)}{A_0(x)} \right)^n \right] + p_e(x,t). \tag{2}$$

Here, $p_e(x,t)$ is a given external pressure, and $K(x)$, m, n, $A_0(x)$ are parameters that take into account mechanical and geometrical properties of the vessel.

Equations (1) must be complemented with appropriate boundary conditions at terminal vertexes of the network and so-called coupling conditions at internal vertexes or junctions. Concerning junctions, if we consider N_P vessels sharing a vertex, we must define N_P state vectors $\mathbf{Q}_*^k$ with $k = 1,\ldots,N_P$ (see (9) below), in order to provide coupling conditions for each one of the vessels converging to the vertex P. A coupling condition is mass conservation

$$\sum_{k=1}^{N_P} g_P^k q_*^k = 0\,, \tag{3}$$

where g_P^k is the auxiliary function

$$g_P^k = \begin{cases} 1\,, & \text{if } x_P^k = L^k\,, \\[2mm] -1\,, & \text{if } x_P^k = 0 \end{cases} \tag{4}$$

and x_P^k is the local coordinate of the k-th edge, evaluated at vertex P. A second coupling condition is given by either total pressure [13]

$$p(A_*^1) + \frac{1}{2}\rho\left(\frac{q_*^1}{A_*^1} \right)^2 - p(A_*^k) - \frac{1}{2}\rho\left(\frac{q_*^k}{A_*^k} \right)^2 = 0\,, \quad k = 2,\ldots,N_P \tag{5}$$

or pressure [24]

$$p(A_*^1) - p(A_*^k) = 0\,, \quad k = 2,\ldots,N_P\,. \tag{6}$$

Since parameters in (2) may vary in space and in the case of a junction could most certainly present discontinuous variations among neighboring domains, we consider the mathematical model and associated RP solver proposed in [21]. Let us first define the following trivial auxiliary equations

$$\partial_t K = 0\,, \quad \partial_t A_0 = 0\,, \quad \partial_t p_e = F(x,t)\,, \tag{7}$$

where $F(x,t)$ is a prescribed function for the external pressure. Then, the modified model is written in quasi-linear form as

$$\partial_t \mathbf{Q} + \mathbf{A}(\mathbf{Q})\partial_x \mathbf{Q} = \mathbf{S}(\mathbf{Q})\,, \tag{8}$$

3

with

$$\mathbf{Q} = \left[A, q, K, A_0, p_e\right]^T,$$ (9)

and coefficient matrix $\mathbf{A}(\mathbf{Q})$

$$\mathbf{A}(\mathbf{Q}) = \begin{bmatrix} 0 & 1 & 0 & 0 & 0 \\ c^2 - u^2 & 2u & \frac{A}{\rho}\phi & K\frac{A}{\rho}\partial_{A_0}\phi & \frac{A}{\rho} \\ 0 & 0 & 0 & 0 & 0 \\ 0 & 0 & 0 & 0 & 0 \\ 0 & 0 & 0 & 0 & 0 \end{bmatrix}.$$ (10)

Here $u = q/A$ is the cross-sectional averaged velocity of the fluid, $\mathbf{S}(\mathbf{Q})$ is a source term vector

$$\mathbf{S}(\mathbf{Q}) = [0, -f/\rho, 0, 0, F(x,t)]^T$$ (11)

and c is the wave speed

$$c = \sqrt{\frac{A}{\rho}K\partial_A\phi}.$$ (12)

For a thorough mathematical analysis of system (8) see [21]. Here we recall some of the main features of the system needed for the construction of the proposed methodology. The eigenvalues of (10) are: $\lambda_1 = u - c, \quad \lambda_2 = \lambda_3 = \lambda_4 = 0, \quad \lambda_5 = u + c$. Moreover, under a suitable assumption for coefficients m and n, system (8) is hyperbolic, though not strictly hyperbolic. Hyperbolicity is lost when $|u| = c$, leading to resonance and thus possible loss of uniqueness. Characteristic fields 1 and 5 are genuinely non-linear and therefore are associated with shocks and rarefactions. The remaining fields are linearly degenerate (LD) and are associated with stationary contact discontinuities.

2.2. RP at a junction for system (8)

Wave relations for all characteristic fields of (8) are provided in [21]. Having this information available, the Riemann problem can be solved by defining wave relations for all characteristic fields and iteratively finding the states connected by admissible waves in phase-space. See [14, 25] for background. Here we formulate the problem and its solution for N_P, infinitely long converging vessels sharing vertex P. The Riemann problem at vertex P reads

$$\begin{cases} \partial_t \mathbf{Q}^k + \mathbf{A}(\mathbf{Q}^k)\partial_x \mathbf{Q}^k = 0, x \in \mathcal{R}, t \rangle 0, \\ \mathbf{Q}^k(x,0) = \mathbf{Q}_{1D}^k, \end{cases}$$ (13)

for $k = 1, \ldots, N_P$.

The self-similar solution to (13) consists of $2N_P$ constant states, where N_P states are the initial condition states provided by the one-dimensional vessels $\mathbf{Q}_{1D}^k$, with $k = 1, \ldots, N_P$, while the remaining states $\mathbf{Q}_*^k$, with $k = 1, \ldots, N_P$, are states connected to initial condition states via non-linear waves and among themselves via the linearly degenerate stationary contact discontinuity created by the discontinuous variation of mechanical and geometrical properties of vessels at vertex P. In general, the unknown state vectors $\mathbf{Q}_*^k, k = 1, \ldots, N_P$ are computed by solving the following non-linear system of $2N_P$ equations

$$\begin{cases} \sum_{k=1}^{N_P} g_P^k A_*^k u_*^k = 0, \\ p(A_*^1) + \frac{1}{2}\rho(u_*^1)^2 - p(A_*^k) - \frac{1}{2}\rho(u_*^k)^2 = 0, \quad k = 2, \ldots, N_P, \\ u_*^k - u_{1D}^k + g_P^k \beta^k = 0 \quad k = 1, \ldots, N_P, \end{cases}$$ (14)

where β^k is

$$\beta^k = \begin{cases} \displaystyle\int_{A_{1D}^k}^{A_*^k} \frac{c(\tau)}{\tau} d\tau & \text{if } A_*^k \langle A_{1D}^k \\[4mm] \displaystyle\sqrt{\frac{B^k (A_*^k - A_{1D}^k)}{A_*^k A_{1D}^k}} & \text{if } A_*^k \geq A_{1D}^k \end{cases} , \tag{15}$$

and B^k is

$$B^k = \frac{K^k}{\rho} \left(\frac{m}{m+1} \frac{(A_*^k)^{m+1} - (A_{1D}^k)^{m+1}}{(A_0^k)^m} - \frac{n}{n+1} \frac{(A_*^k)^{n+1} - (A_{1D}^k)^{n+1}}{(A_0^k)^n} \right). \tag{16}$$

Full details on the derivation of wave relations present in (14), obtained by a standard eigen-structure analysis of (8), are given in [21]. It is worth noting that the first N_P wave relations are related to the stationary contact discontinuity generated by variable mechanical and geometrical properties, while the remaining relations are valid across non-linear waves.

2.3. Accurate GRP solution via the Dumbser-Enaux-Toro solver

The GRP has to be solved at both, internal cell interfaces, *i.e.* within the one-dimensional domain, as well as at boundary cell interfaces. It is therefore appropriate to introduce the numerical methodology used to solve the GRP in the one-dimensional domain and then illustrate how to treat this problem in correspondence of internal vertexes.

2.3.1. Path-conservative finite-volume-type numerical scheme

We adopt a path-conservative finite-volume type numerical scheme of the form

$$\mathbf{Q}_i^{n+1} = \mathbf{Q}_i^n - \frac{1}{\Delta x_i} \int_{t^n}^{t^{n+1}} \int_{x_{i-\frac{1}{2}}}^{x_{i+\frac{1}{2}}} \mathbf{A}(\mathbf{Q}) \partial_x \mathbf{Q} \, dx \, dt - \frac{\Delta t^n}{\Delta x_i} \left(\mathbf{D}_{i+\frac{1}{2}}^- + \mathbf{D}_{i-\frac{1}{2}}^+ \right) + \Delta t^n \mathbf{S}_i , \tag{17}$$

for $i = 1,\dots,N$, where N is the number of computational cells, $\Delta x_i = x_{i+\frac{1}{2}} - x_{i-\frac{1}{2}}$ is the mesh spacing and $\Delta t^n = t^{n+1} - t^n$ is the time step. Moreover, we have

$$\mathbf{Q}_i^n = \frac{1}{\Delta x_i} \int_{x_{i-\frac{1}{2}}}^{x_{i+\frac{1}{2}}} \mathbf{Q}(x,t^n) \, dx , \tag{18}$$

$$\mathbf{S}_i = \frac{1}{\Delta t^n \Delta x_i} \int_{t^n}^{t^{n+1}} \int_{x_{i-\frac{1}{2}}}^{x_{i+\frac{1}{2}}} \mathbf{S}(\mathbf{Q}(x,t)) \, dx \, dt \tag{19}$$

and

$$\mathbf{D}_{i+\frac{1}{2}}^{\pm} = \frac{1}{\Delta t^n} \int_{t^n}^{t^{n+1}} \mathcal{D}_{i+\frac{1}{2}}^{\pm} \left(\mathbf{Q}_{i+\frac{1}{2}}^-(t), \mathbf{Q}_{i+\frac{1}{2}}^+(t), \Psi \right) dt . \tag{20}$$

Here $\mathbf{Q}_{i+\frac{1}{2}}^{\pm}(t)$ are limiting data states from left and right arising from the solution of the GRP for system (8) at cell interface $x_{i+\frac{1}{2}}$ and $\mathcal{D}_{i+\frac{1}{2}}^{\pm} \left(\mathbf{Q}_{i+\frac{1}{2}}^-(t), \mathbf{Q}_{i+\frac{1}{2}}^+(t), \Psi \right)$ is a monotone first order fluctuation [26] defined as

$$\mathcal{D}_{i+\frac{1}{2}}^{\pm} = \frac{1}{2} \int_0^1 \left[\mathbf{A}(\Psi(\mathbf{Q}_{i+\frac{1}{2}}^-, \mathbf{Q}_{i+\frac{1}{2}}^+, s)) \pm |\mathbf{A}(\Psi(\mathbf{Q}_{i+\frac{1}{2}}^-, \mathbf{Q}_{i+\frac{1}{2}}^+, s))| \right] \frac{\partial \Psi}{\partial s} \, ds , \tag{21}$$

where the path $\Psi = \Psi(\mathbf{Q}^-, \mathbf{Q}^+, s)$, with $0 \leq s \leq 1$, is a Lipschitz continuous function that connects the left state $\mathbf{Q}^-$ to the right state $\mathbf{Q}^+$ in phase-space, satisfying

$$\Psi\left(\mathbf{Q}^-, \mathbf{Q}^+, 0\right) = \mathbf{Q}^-, \ \ \Psi\left(\mathbf{Q}^-, \mathbf{Q}^+, 1\right) = \mathbf{Q}^+. \tag{22}$$

For full details on the computation of first order fluctuations the reader is referred to [10] and references therein. For $\mathbf{D}^\pm_{i-\frac{1}{2}}$, analogous definitions to (20)-(21) hold.

In order to achieve high order accuracy in space and time, integrals in (17) have to be computed in a proper manner. This involves the computation of both, space-time evolution of the state vector within the control volume $[x_{i-\frac{1}{2}}, x_{i+\frac{1}{2}}] \times [t^n, t^{n+1}]$ and time integrals along cell interfaces. We use the Dumber-Enaux-Toro (DET) solver, proposed in [18] and extended to non-conservative systems in [27, 28].

2.3.2. Spatial reconstruction

As we shall see later in this section, the DET solver, as many high order finite volume solvers, requires a spatial reconstruction procedure based on cell averages. In this work we use the Weighted Essentially Non-Oscillatory (WENO) methodology proposed in [29]. This spatial reconstruction procedure differs from the original WENO methodology [20, 30] in that entire spatial polynomials over the computational cell are obtained. First we introduce reference coordinates $0 \leq \xi \leq 1$ given by $x = x_{i-\frac{1}{2}} + \xi \Delta x_i$. For a scheme of order k, at each time level t^n, we reconstruct element-wise polynomials of the type

$$\mathbf{w}_i = \mathbf{w}_i(\xi, t^n) = \sum_{l=1}^{M+1} \psi_l(\xi) \hat{\mathbf{w}}_l(t^n) := \psi_l(\xi) \hat{\mathbf{w}}_l(t^n), \tag{23}$$

where $M = k - 1$ is the polynomial degree of the spatial reconstruction, $\psi_l(\xi)$, $l = 1, \ldots, M+1$, are the corresponding basis functions and $\hat{\mathbf{w}}_l(t^n)$, $l = 1, \ldots, M+1$, are the expansion coefficients at time $t = t^n$. Note that in (23) we have introduced the Einstein summation convention, which implies summation over repeated indexes. This convention will be used throughout the rest of this work.

The spatial reconstruction is performed on a set of stencils defined as

$$\mathcal{S}_i^s = \bigcup_{e=i-L}^{i+R} T_e, \tag{24}$$

where $L = L(M, s)$ and $R = R(M, s)$ are the stencil extent to the left and to the right, respectively. For odd order schemes we use three stencils, one central stencil ($s = 1$, $L = R = M/2$), a fully left-sided stencil ($s = 2$, $L = M$, $R = 0$) and a fully-right sided stencil ($s = 3$, $L = 0$, $R = M$). For even order schemes we use four stencils, two of which are central ($s = 0$, $L = floor(M/2) + 1$, $R = floor(M/2)$) and ($s = 1$, $L = floor(M/2)$, $R = floor(M/2) + 1$), and two fully left- and right-sided as defined before.

Details on the spatial reconstruction are omitted since the methodology is rather standard and was extensively documented in the literature. For details on the particular WENO version used in this paper see [29, 31].

A further aspect to be addressed emerges from the fact that for any order of accuracy greater than 1, there will be cells of the spatial reconstruction stencil that fall outside the one-dimensional domain. These cells are commonly called *ghost* cells. This aspect will be treated in Section 2.3.5, after the GRP solution is fully described.

2.3.3. Space-time implicit discontinuous Galerkin prediction

A key feature of the DET solver is the time evolution of the initial data left and right of the interface $x_{i+\frac{1}{2}}$. To this end, a space-time local Discontinuous-Galerking (DG) scheme is used, which will provide a local space-time polynomial $\mathbf{Q}_h$ to be later used to solve integrals in (17). We start by transforming system (8) to a reference space-time element $T_E = [0,1] \times [0,1]$ with reference coordinates ξ and τ, related to the physical domain by $x = x_{i-\frac{1}{2}} + \Delta x_i \, \xi$ and $t = t^n + \Delta t^n \, \tau$. The resulting system reads

$$\partial_\tau \mathbf{Q}_h + \mathbf{A}^* \partial_\xi \mathbf{Q}_h = \mathbf{S}^*, \tag{25}$$

with modified Jacobian and source term vector

$$\mathbf{A}^* := \frac{\Delta t^n}{\Delta x_i} \mathbf{A}(\mathbf{Q}_h), \quad \mathbf{S}^* := \Delta t^n \mathbf{S}(\mathbf{Q}_h).$$

In order to simplify the notation, we introduce the following operators:

$$[a,b]^\tau = \int_0^1 a(\xi,\tau) b(\xi,\tau) d\xi, \quad \langle a,b \rangle_{T_E} = \int_0^1 \int_0^1 a(\xi,\tau) b(\xi,\tau) d\xi d\tau. \tag{26}$$

Next, we multiply (25) by a space-time basis function $\theta = \theta(\xi,\tau)$ and integrate over the reference element T_E. Using integration by parts for the time derivative term we obtain

$$[\theta, \mathbf{Q}_h]^1 - \langle \partial_\tau \theta, \mathbf{Q}_h \rangle_{T_E} + \langle \theta, \mathbf{A}^* \partial_\xi \mathbf{Q}_h \rangle_{T_E} = [\theta, \mathbf{w}_h]^0 + \langle \theta, \mathbf{S}^* \rangle_{T_E}. \tag{27}$$

We use the same space-time basis functions θ, to approximate $\mathbf{Q}_h$, $\mathbf{A}^* \partial_\xi \mathbf{Q}_h$ and $\mathbf{S}^*$, so that

$$\mathbf{Q}_h(\xi,\tau) = \sum_{l=1}^{(M+1)^2} \theta_l \hat{\mathbf{Q}}_l, \quad \mathbf{A}^* \partial_\xi \mathbf{Q}_h(\xi,\tau) = \sum_{l=1}^{(M+1)^2} \theta_l \widehat{\mathbf{A}^* \partial_\xi \mathbf{Q}}_l, \quad \mathbf{S}^*(\xi,\tau) = \sum_{l=1}^{(M+1)^2} \theta_l \widehat{\mathbf{S}^*}_l, \tag{28}$$

where $\widehat{\mathbf{S}^*}_l = \Delta t^n \mathbf{S}(\hat{\mathbf{Q}}_l)$.

We obtain expansion coefficients $\hat{\mathbf{Q}}_l$ by a fixed point iteration procedure, see [18] for details, in which at each iteration step, $m = 0,1,\ldots$ until convergence is achieved, we solve the following system

$$\left([\theta_k, \theta_l]^1 - \langle \partial_\tau \theta_k, \theta_l \rangle_{T_E}\right) \hat{\mathbf{Q}}_l^{m+1} - \langle \theta_k, \theta_l \rangle_{T_E} \widehat{\mathbf{S}^*}_l^{m+1} = [\theta_k, \psi_l]^0 \hat{\mathbf{w}}_l - \langle \theta_k, \theta_l \rangle_{T_E} \widehat{\mathbf{A}^* \partial_\xi \mathbf{Q}}_l^m, \tag{29}$$

for $k = 1,2,\ldots,(M+1)^2$.

The initial guess for the fixed point iteration procedure is provided by the spatial reconstruction polynomial, so that for $m = 0$ the space-time prediction polynomial is constant in time. For more sophisticated initial guesses see [31]. Having computed the space-time predictions in all computational cells, the solution to the GRP at time t is found by solving a classical Riemann problem using the space-time reconstructed states extrapolated to both sides of the cell interface, see [32]. The source term space-time average (19) and the non-conservative product space-time average present in (17) are computed by numerical integration using $\mathbf{Q}_h$ and a quadrature rule of appropriate accuracy. For space polynomials $\mathbf{w}$ and space-time polynomials $\mathbf{Q}_h$, we adopt a nodal basis function, where space and space-time nodes are given by Gaussian quadrature points and the space and space-time basis functions are the Lagrange interpolation polynomials passing through these points [31].

2.3.4. Computation of high-order numerical fluxes/fluctuations at boundary cell interfaces

In the case of boundary cell interfaces, one has to solve a *classical* RP at the internal vertex P with N_P predicted states, as shown in Section 2.2. As in the case of internal cell interfaces, *i.e.* within the one-dimensional domain, these RPs have to be solved at appropriate quadrature points for time integration in (20).

For hyperbolic systems written in conservation form, the numerical flux is directly computed, since the solution of the RP at quadrature points provides the Godunov state used to evaluate the physical flux. On the other hand, in the case of non-conservative systems a fluctuation has to be computed. In the case of a positive fluctuation at an inflow boundary cell interface located at $x = 0$, it is sufficient to perform the integral in (21) as

$$\mathbf{D}^+_{1-\frac{1}{2}} = \frac{1}{\Delta t^n} \int_{t^n}^{t^{n+1}} \mathcal{D}^{\pm}_{1-\frac{1}{2}}\left(\mathbf{Q}^-_*(t), \mathbf{Q}^+_{1-\frac{1}{2}}(t), \Psi\right) dt,\tag{30}$$

where $\mathbf{Q}^-_*(t)$ is the solution to the classical RP for initial conditions given by predicted space-time polynomials evaluated at time t on the corresponding internal vertex. Similarly, for an outflow boundary cell interface located at $x = L$, with L the length of the edge, it is sufficient to perform the integral in (21) using the predicted state and the Godunov state as follows:

$$\mathbf{D}^-_{N+\frac{1}{2}} = \frac{1}{\Delta t^n} \int_{t^n}^{t^{n+1}} \mathcal{D}^{\pm}_{N+\frac{1}{2}}\left(\mathbf{Q}^-_{N+\frac{1}{2}}(t), \mathbf{Q}^+_*(t), \Psi\right) dt.\tag{31}$$

See [33, 34] for details on the design of the integration path Ψ when an exact RP solver is used.

2.3.5. Ghost cell filling for spatial reconstruction

At time t^n, the WENO procedure requires M ghost cells to be filled at each side of the one-dimensional edge. In practice, an accurate approximation of the solution is required in order to compute cell averages that will then be used to fill ghost cells. Here, we propose a methodology that is similar to the one presented in [16]. The solution approximation used to compute cell averages is provided by a Taylor series expansion around the internal vertex P, shared by the k-th edge. Assuming that the origin of a local spatial coordinate ε is located at the internal vertex P, shared by the k-th edge, the state vector outside the one-dimensional domain for the this edge has the form

$$\mathbf{Q}^k_g(\varepsilon, t^n) = \mathbf{Q}^k_*(t^{n-1} + \Delta t^{n-1}) + \sum_{j=1}^{M} \frac{1}{j!} \partial_x^{(j)} \mathbf{Q}^k_*(t^{n-1} + \Delta t^{n-1})\, \varepsilon^j,\tag{32}$$

where $\mathbf{Q}^k_*(t^{n-1} + \Delta t^{n-1})$ is the solution of the GRP for the k-th edge sharing vertex P, obtained from the previous time step. For the case $n = 0$, the initial condition is used to assign $\mathbf{Q}^k_*(t^{n-1} + \Delta t^{n-1})$ and its spatial derivatives.

In [16], $\partial_x^{(j)} \mathbf{Q}^k_*(t^{n-1} + \Delta t^{n-1})$ was approximated by performing an inverse Cauchy-Kowalewski procedure, such that spatial derivatives could be computed from temporal derivatives available from the GRP solution of the previous time step. Here, we directly use the spatial derivatives from the implicit DG prediction of the previous time step. To compute spatial derivatives out of the space-time prediction $\mathbf{Q}_h(\xi, \tau)$, we recursively make the following *ansatz*

$$\langle \theta_k, \theta_l \rangle \widehat{\partial_\xi^{(j)} \mathbf{Q}}_l = \langle \theta_k, \partial_\xi \theta_l \rangle \widehat{\partial_\xi^{(j-1)} \mathbf{Q}}_l,\tag{33}$$

with $j = 1, \ldots, M$ and $k, l = 1, 2, \ldots, (M+1)^2$. Note that matrix $\langle \theta_k, \theta_l \rangle^{-1} \langle \theta_k, \partial_\xi \theta_l \rangle$ is computed only once, so that the spatial derivatives are obtained by a simple matrix-vector product. Moreover, it is worth mentioning that avoiding the use of the inverse Cauchy-Kowalewski procedure allows to apply this procedure to hyperbolic systems with non-invertible Jacobian matrixes.

2.4. Summary of the algorithm

Consider a network consisting of N_V vertexes and N_E edges. N_I are internal vertexes or junctions and $N_B = N_V - N_I$ terminal nodes on which boundary conditions must be provided. The following list summarizes how to evolve the solution from time t^n to t^{n+1}:

1. For all edges: fill ghost cells for spatial reconstruction as specified in Section 2.3.5 and perform WENO as stated in Section 2.3.2.
2. For all edges: perform the prediction step as specified in Section 2.3.3.
3. For all internal vertexes or junctions: solve the *classical* RP for appropriate time integration quadrature points as described in Section 2.2.
4. For all internal cell interfaces of all edges: compute fluctuations using (20) with first order fluctuations (21).
5. For all boundary cell interfaces of all edges: compute fluctuations using (20) with first order fluctuations (30) and (31).
6. For all edges: update the solution using (17).

3. Results

In this section we perform a series of tests in order to verify the accuracy and robustness of the methodology presented in the previous section. For all tests presented here, the vessel stiffness coefficient K is computed, following [8], as

$$K(x) = \frac{4}{3} \frac{h E}{R_0(x)}, \tag{34}$$

where h is the vessel wall thickness, E is the effective Young modulus of the vessel wall material and R_0 is the radius of the reference cross-sectional area A_0. Note that a variation of A_0 in space will cause a variation of the vessel stiffness coefficient K.

3.1. Convergence rates

Here we carry out a convergence rate study in order to verify that the expected theoretical order of accuracy of the proposed numerical scheme is actually attained. To this end we construct a test problem for a modified non-linear system of equations that is a perturbation of the original system via a source term vector. In this manner we obtain a smooth, exact solution of a non-homogeneous non-linear system. We proceed to prescribe a smooth function $\hat{\mathbf{Q}}(x, t)$ that will be the exact solution of the perturbed system. Here we choose

$$\hat{\mathbf{Q}}(x,t) = \begin{bmatrix} \hat{A}(x,t) \\ \hat{q}(x,t) \end{bmatrix} = \begin{bmatrix} A^c + \delta_A A^c \sin\left(\frac{2\pi}{L}x\right)\cos\left(\frac{2\pi}{T_0}t\right) \\ q^c - \delta_A A^c \frac{L}{T_0} \cos\left(\frac{2\pi}{L}x\right)\sin\left(\frac{2\pi}{T_0}t\right) \end{bmatrix}, \tag{35}$$

where quantities with superscript c are average values and terms δ are fluctuations around the average. Inserting (35) into (8) we obtain the following inhomogeneous system

$$\partial_t \mathbf{Q} + \mathbf{A}(\mathbf{Q})\partial_x \mathbf{Q} = \mathbf{S}(\mathbf{Q}) + \hat{\mathbf{S}}(x,t). \tag{36}$$

The resulting source term $\hat{\mathbf{S}}(x, t)$ reflects the fact that (35) is not a solution of the original system (8). $\hat{\mathbf{S}}(x, t)$ can be calculated using algebraic manipulators; its expression is not reproduced here.

The convergence test is performed over a network composed by two vessels connected at both extremities, thus forming a closed loop. The number of cells used in each mesh refinement step

in one of the vessels is always the double of the quantity used in the other one. Reference parameters are: $h = 0.5\,mm$, $R_0 = 14\,mm$, $E_E = 1.2\,MPa$, $p_0 = 0\,Pa$, $\mu = 0\,Pa\,s$. Moreover, the following parameters are used: $L = 1.0\,m$, $T_0 = 1\,s$, $A^c = \pi R_0^2$, $\delta_A = 0.1$, $q^c = 100\,ml\,s^{-1}$. The output time is taken as $t_{\mathrm{end}} = 0.5\,s$ and the CFL number used is $CFL = 0.9$.

Table 1 displays the empirical convergence rates for second and third order versions of the proposed finite volume-type numerical scheme, respectively. Errors for the cross-sectional area were measured in the norms L^1, L^2 and L^∞. The expected convergence rates are reached for all norms, even with reduced number of computational cells discretizing the domain.

Throughout this work we will denote as *J1*, numerical solutions obtained by performing WENO considering constant data on ghost cells and by using only constant (in time) states at t^n as initial conditions for the Riemann problem at the junction instead of predicted states provided by the DET solver. High order coupling as proposed in the present work is denoted by *JN*, with N the order of accuracy of the coupling strategy. Convergence rates for low order coupling are also shown in Table 1, illustrating that the formal order of accuracy is lost in this case, as expected.

Test	N	L^1	L^2	L^∞	$\mathcal{O}(L^1)$	$\mathcal{O}(L^2)$	$\mathcal{O}(L^\infty)$
ADER-O2-J2	4	1.65e-05	1.92e-05	4.67e-05	-	-	
	8	3.77e-06	4.65e-06	1.48e-05	2.1	2.0	1.7
	16	8.81e-07	1.09e-06	3.66e-06	2.1	2.1	2.0
	32	2.31e-07	2.88e-07	9.55e-07	1.9	1.9	1.9
	64	6.11e-08	7.53e-08	2.31e-07	1.9	1.9	2.1
ADER-O3-J3	4	6.03e-06	8.32e-06	1.90e-05	-	-	
	8	1.08e-06	1.42e-06	3.36e-06	2.5	2.6	2.5
	16	1.22e-07	1.59e-07	4.57e-07	3.1	3.2	2.9
	32	1.50e-08	1.91e-08	5.45e-08	3.0	3.1	3.1
	64	1.94e-09	2.43e-09	6.79e-09	3.0	3.0	3.0
ADER-O2-J1	4	2.01e-05	2.32e-05	5.35e-05	-	-	
	8	6.20e-06	8.03e-06	2.49e-05	1.7	1.5	1.1
	16	1.88e-06	2.91e-06	1.44e-05	1.7	1.5	0.8
	32	6.35e-07	1.08e-06	7.44e-06	1.6	1.4	1.0
	64	2.62e-07	4.22e-07	3.79e-06	1.3	1.4	1.0
ADER-O3-J1	4	1.38e-05	1.63e-05	3.16e-05	-	-	
	8	4.43e-06	7.02e-06	2.53e-05	1.6	1.2	0.3
	16	1.42e-06	2.65e-06	1.43e-05	1.6	1.4	0.8
	32	5.42e-07	1.02e-06	7.54e-06	1.4	1.4	0.9
	64	2.54e-07	4.20e-07	3.83e-06	1.1	1.3	1.0

Table 1: Empirical convergence rates obtained for second and third order ADER schemes. N is the number of cells of the vessel with the coarsest mesh. Errors are computed for variable $A\,[m^2]$ and refer to the vessel with the coarsest mesh.

3.2. Wave propagation in a simple network

In order to study the effect of the proposed coupling strategy on numerical results, we consider a simple vessel network composed by three vessels, with properties defined in Table 2. Vessel 1 is the parent vessel, whereas vessels 2 and 3 are daughter vessels. It is worth noting that the reference cross-sectional area of the vessels that compose the network are different, with discontinuous variation at the bifurcation point. Moreover, spatial discretization is different in each vessel. Other relevant parameters are: $\mu = 0\,Pa\,s$; $\rho = 1050\,kg\,m^{-3}$, $E = 1.2\,MPa$, $h = 0.5\,mm$. A CFL number of $CFL = 0.9$ was used for all computations reported in this section.

3.2.1. Smooth wave

In this test we prescribe the flow rate curve reported in [8] at the beginning of vessel 1, whereas the ends of vessels 2 and 3 are considered as transparent boundaries. Initial conditions are $p(x,0) = 10.656\,KPa$ and $q(x,0) = 0\,ml\,s^{-1}$.

Vessel no.	$L\,[mm]$	$r_0\,[mm]$	$\Delta x\,[mm]$
1	500	14	10
2	500	10	20
3	500	7	30

Table 2: Parameters for vessel network used in Section 3.2.

The solution for time $t = 0.12\,s$ is shown in Figure 1. Results for pressure and flow include a reference solution obtained with a first order scheme on a very fine mesh ($\Delta x = 1\,mm$), as well as second and third order solutions for both, high and low order coupling schemes. Daughter vessel 3 is not displayed for the sake of clarity. From the presented results it can be easily concluded that the high order coupling yields a more accurate solution than the low order coupling.

3.2.2. Shock wave

Here we assess the ability of the proposed methodology to solve problems involving the propagation of discontinuities in a network. This is perhaps not relevant for arterial blood flow, but could be a situation that might be observed in other physiological flows, such as in the respiratory system [35] or in the venous system [36].

Test 1

In this test all outlets of the network are considered to be transparent boundaries. Initial conditions are identical to the ones used for the previous test, except for pressure in vessel 1, where we prescribe $p_1(x,0) = 11.988\,KPa$ for $x < 0.4\,m$.

The solution for time $t = 0.06\,s$ is shown in Figure 2. Results for pressure and flow include a reference solution obtained with a first order scheme on a very fine mesh ($\Delta x = 1\,mm$), as well as second and third order solutions for both, high and low order coupling. The initial pressure discontinuity generates a forward-traveling shock and a backward-traveling rarefaction. As the shock reaches the bifurcation point, it propagates through both daughter vessels. Moreover, a reflected shock is generated in vessel 1. The better accuracy of high order coupling is not as evident as for the smooth case, even if results for high order coupling are slightly more accurate. This can be explained by the fact that the shock is enforcing the spatial reconstruction to lower the order of the solution at the shock.

Test 2

In order to further assess the capacity of the proposed reconstruction procedure to deliver (essentially) non-oscillatory solutions, we now consider a test case in which the pressure discontinuity is located in one of the daughter vessels. In particular, initial pressure in vessel 2 is set to $p_2(x,0) = 11.988\,KPa$ for $x > 0.15\,m$. The obtained solutions for $t = 0.08\,s$ are shown in Figure 3. In this case the initial pressure discontinuity produces a backward-traveling shock and a forward-traveling rarefaction, which for the displayed time has already abandoned the vessel. As the shock reaches the bifurcation a forward-traveling rarefaction is generated in vessel 2, while the shock propagates in vessels 1 and 2.

3.3. Arterial network

Here we consider the model of the human arterial system presented in [37] and further studied in [8]. The model includes 37 major arteries, an inflow curve at the root of the aorta and terminal resistances, as shown in Figure 4. For full details on the model see [37] and [8].

The vessels included in the model present tapering and discontinuous variations of geometrical and mechanical properties across junctions, being therefore perfectly suited to validate the proposed methodology.
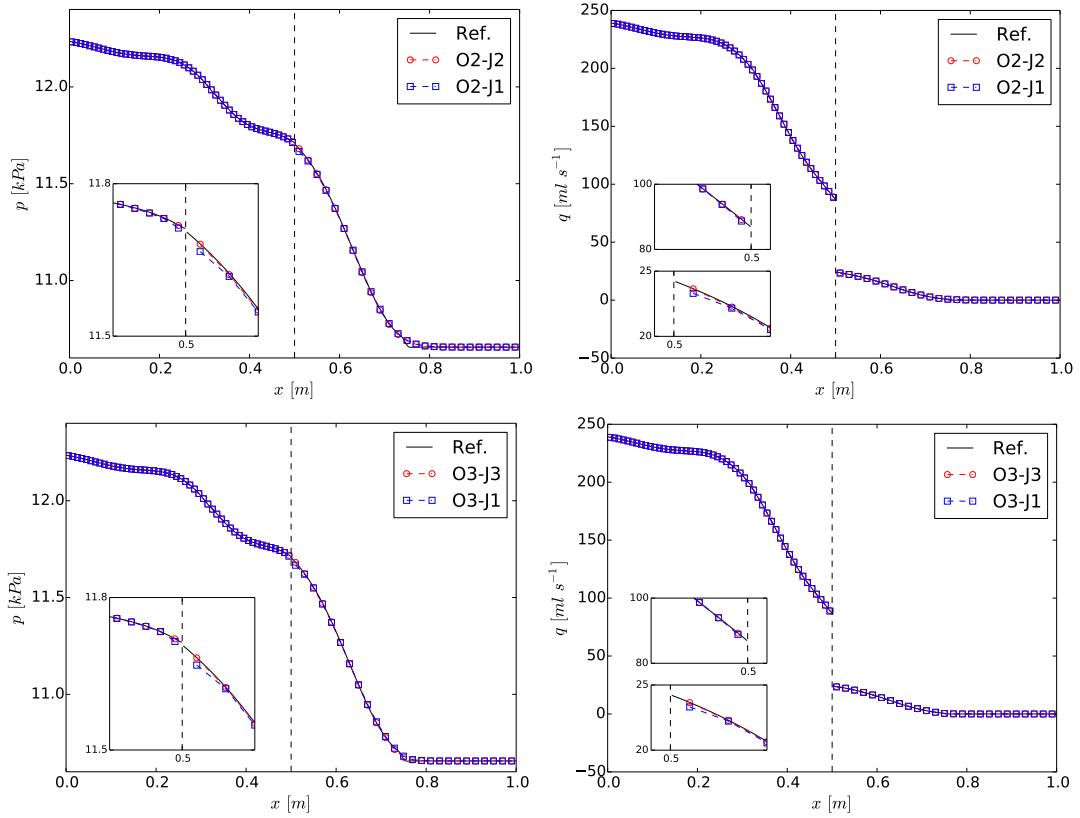
Figure 1: Smooth wave in a simple network at time $t = 0.12\,s$. Vertical dashed line shows the location of the junction. Daughter vessel 3 is not displayed for the sake of clarity. Insets display the solution at the junction. *Ref.* was obtained using a first order scheme on a very fine mesh ($\Delta x = 1\,mm$).
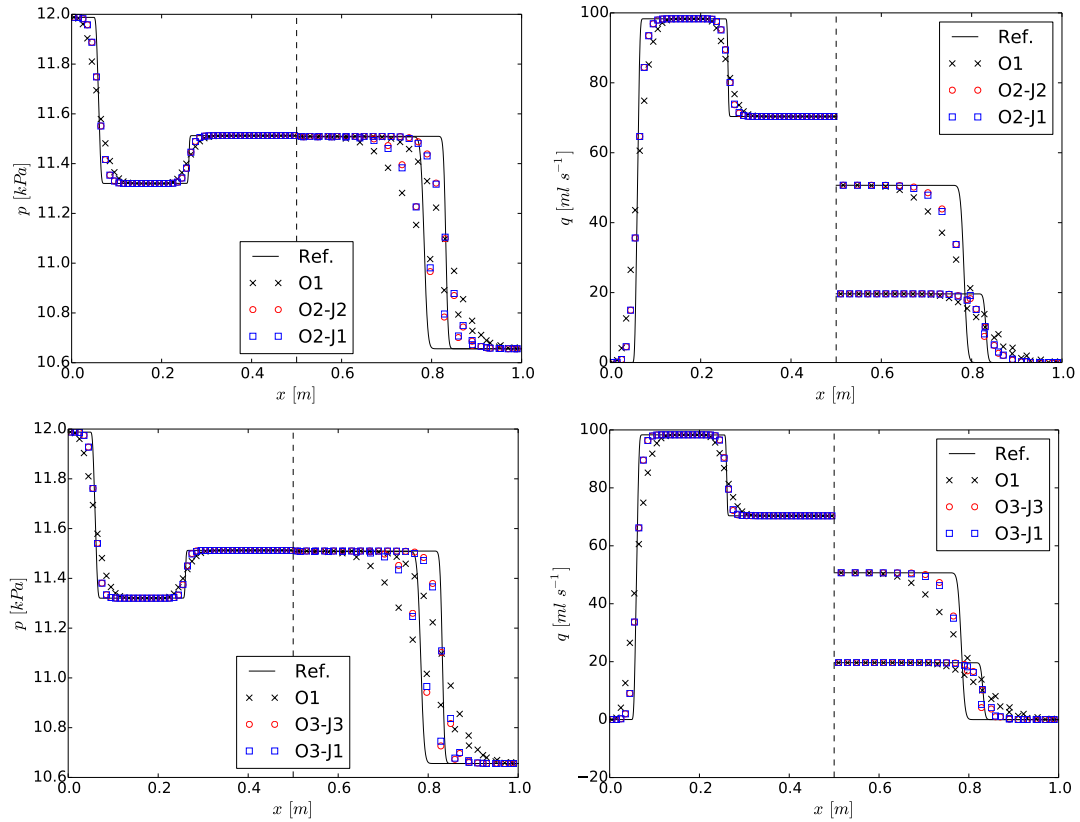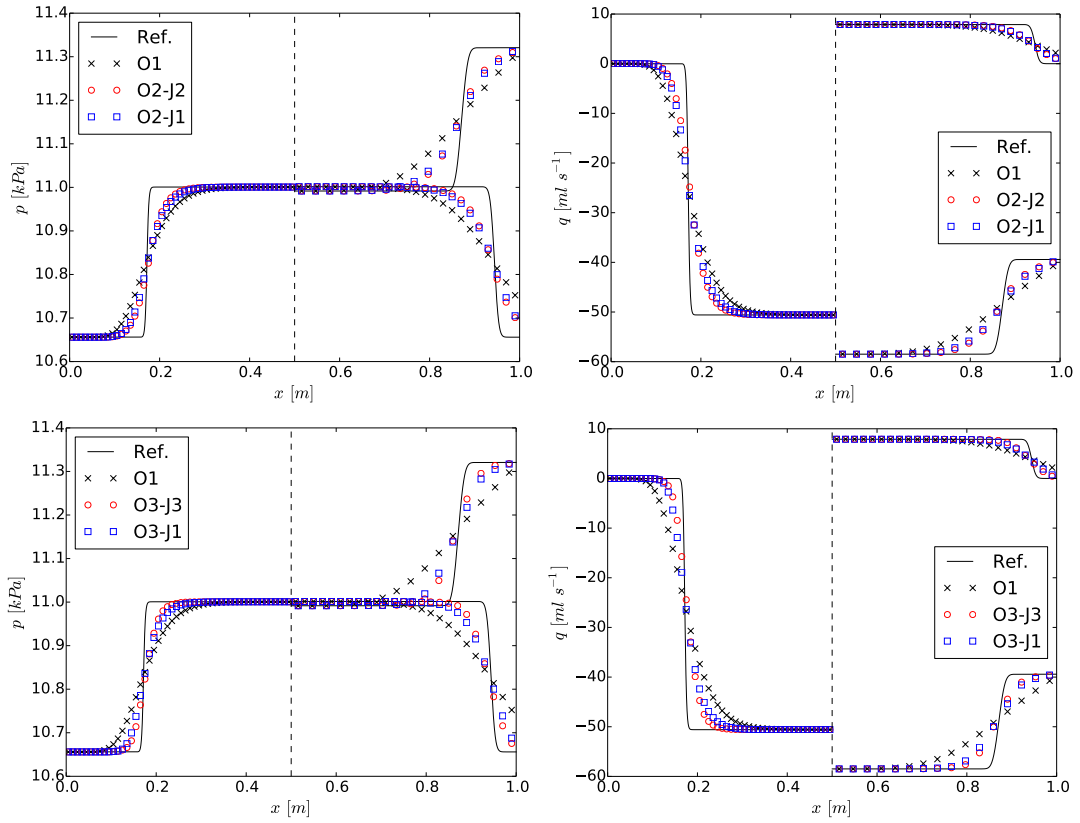
Figure 2: Shock wave in a simple network: test 1. Second and third order results for pressure and flow. Output time $t = 0.06\,s$. The solution in vessel 3 is the one where the shock wave has advanced more in space. *Ref.* was obtained using a first order scheme on a very fine mesh ($\Delta x = 1\,mm$).

13

Figure 3: Shock wave in a simple network: test 2. Second and third order results for pressure and flow. Output time $t = 0.08\,s$. *Ref.* was obtained using a first order scheme on a very fine mesh ($\Delta x = 1\,mm$).
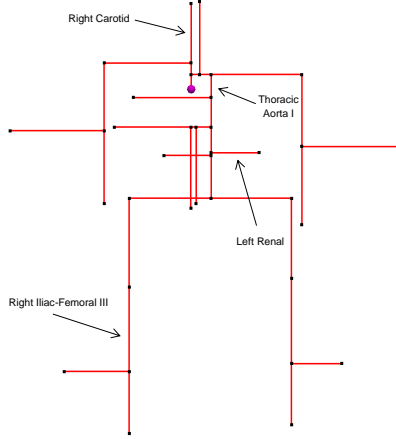
Figure 4: Schematic representation of the *in vitro* model of the arterial system presented in [37]. Purple dot represent the network inlet, black dots are junctions or terminal nodes. A pump is connected to the network inlet and resistances are connected to terminal segments. Arrows indicate vessels for which the solution is displayed. For full details on the network topology and geometrical/mechanical parameters refer to [8, 37].

The number of computational cells used in the j-th vessel is defined as $N_j = \lceil \frac{L_j}{\Delta x_{\max}} \rceil$. Computations were performed using a $CFL = 0.9$ on a notebook with an Intel Core i7-4500 (1.80 GHz clock speed). Table 3 reports setting details of the runs for which computational results shown in this section were obtained.

Label	$\Delta x_{\max} [mm]$	$Order-1D$	$Order-Junction$	$t_{CPU} [s]$
O1	20	1	J1	10.07
O1-RFN1	10	1	J1	17.24
O1-RFN2	5	1	J1	36.18
Ref.	1	1	J1	794.00
O2-J2	20	2	J2	12.04
O2-J1	20	2	J1	11.13
O3-J3	20	3	J3	35.30
O3-J1	20	3	J1	20.24

Table 3: Setting of simulations for computational results shown in Section 3.3. t_{CPU} is the computational time per cardiac cycle.

Figures 5 and 6 show computational results for pressure and flow rate. The improvement in the description of waveform landmarks given by the solutions obtained using high order coupling is evident for both quantities, pressure and flow. The improvement is more evident in the case of vessels where flow is highly oscillatory, like the left renal and carotid arteries. However, differences can also be encountered in other vessels, like in the thoracic aorta.

Figure 7 features pressure and flow rate along the aorta and left lower limb for time $t = 10\,s$, which corresponds to nearly maximum flow rate at the root of the aorta. The better approximation

15

obtained by second and third order schemes using a consistent high order coupling is also evident in this complex network. Moreover, from Figure 7 it can be concluded that there is a clear sense of convergence when moving from second to third order coupling, while it is not clear that the same holds for the low order coupling. Remarkably, it could also be noticed that the low order coupling can produce non-physical oscillations in the solution, as shown in Figure 8.

Table 3 shows CPU time per cardiac cycle for all simulations shown in this section. Although these numbers must be considered carefully since the code was not optimized, we can safely conclude that high order schemes are more efficient if a specific accuracy is to be achieved.

4. Final remarks

We have proposed a methodology for a high order approximation of hyperbolic conservation laws in networks. The proposed strategy requires the availability of an exact or approximate Riemann solver for the Riemann problem at a junction and the use of the Dumber-Enaux-Toro solver. The methodology was illustrated for a one-dimensional blood flow model that considers discontinuous variations of mechanical and geometrical properties of vessels. Reported computational results show that the proposed method is crucial to fully exploit the accuracy of high order finite volume schemes.

It is important to stress that the high order approximation proposed here can be applied to any hyperbolic conservation law, conservative or non conservative and possibly with discontinuous flux functions, as long as an exact or approximate Riemann problem solver is available. Moreover, this kind of treatment of internal vertexes is mandatory if local time stepping techniques are to be implemented. This last aspect is being currently investigated.
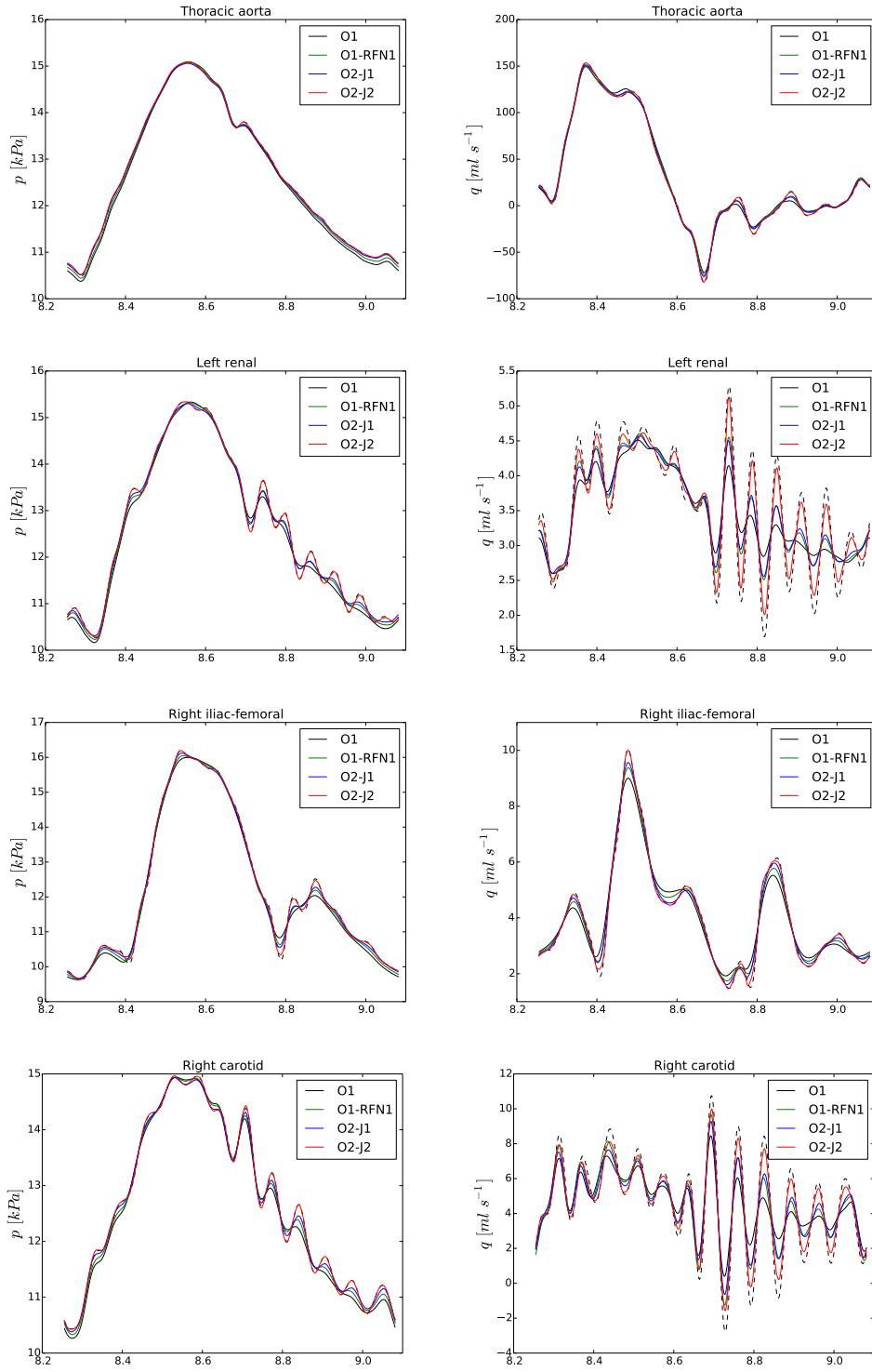
Figure 5: First and second order computational results for pressure and flow. Dashed line refers to a reference solution obtained with a first order scheme and $\Delta x = 1\,mm$. For other quantities refer to Table 3.
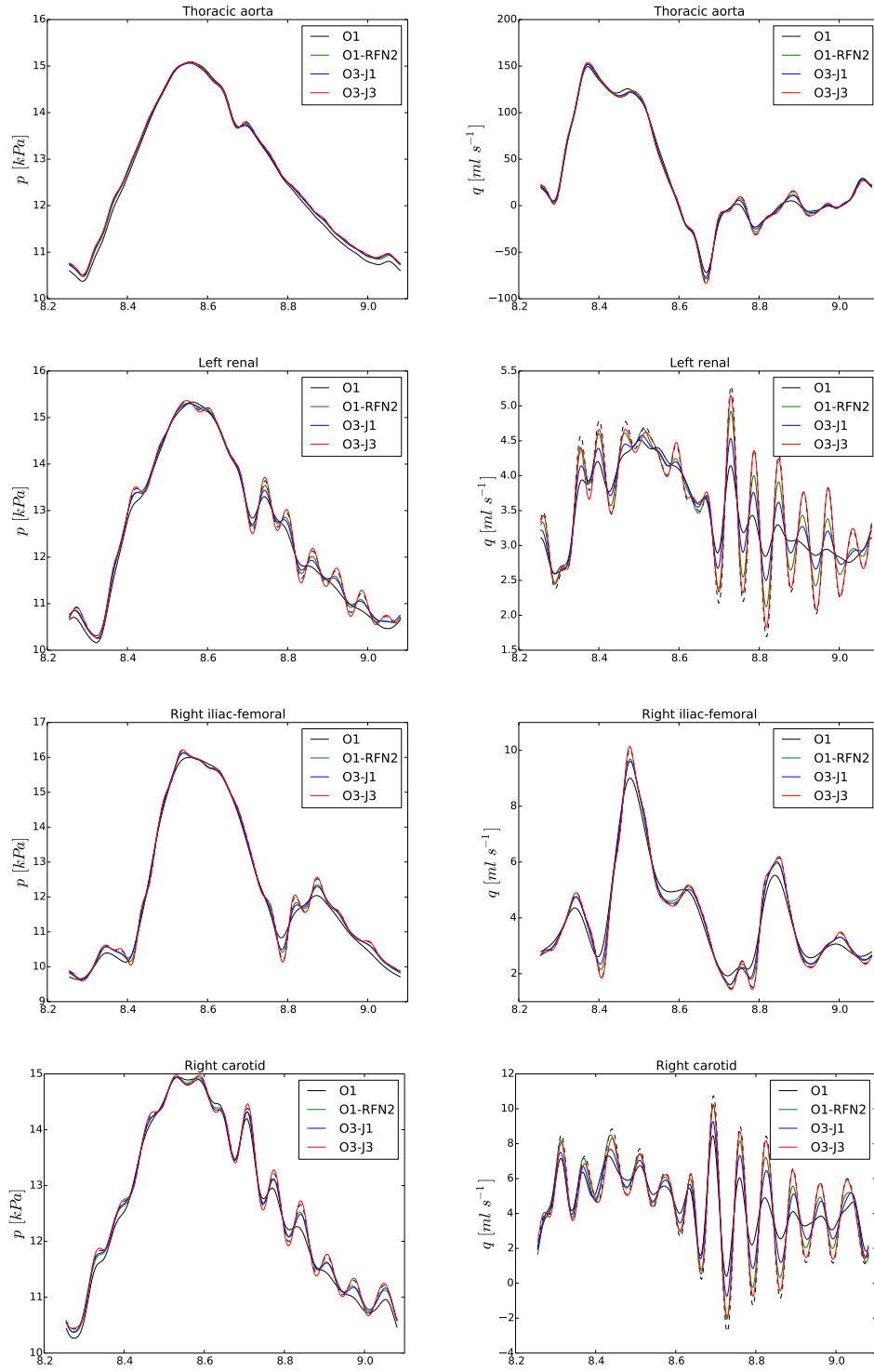
Figure 6: First and third order computational results for pressure and flow. Dashed line refers to a reference solution obtained with a first order scheme and $\Delta x = 1\,mm$. For other quantities refer to Table 3.
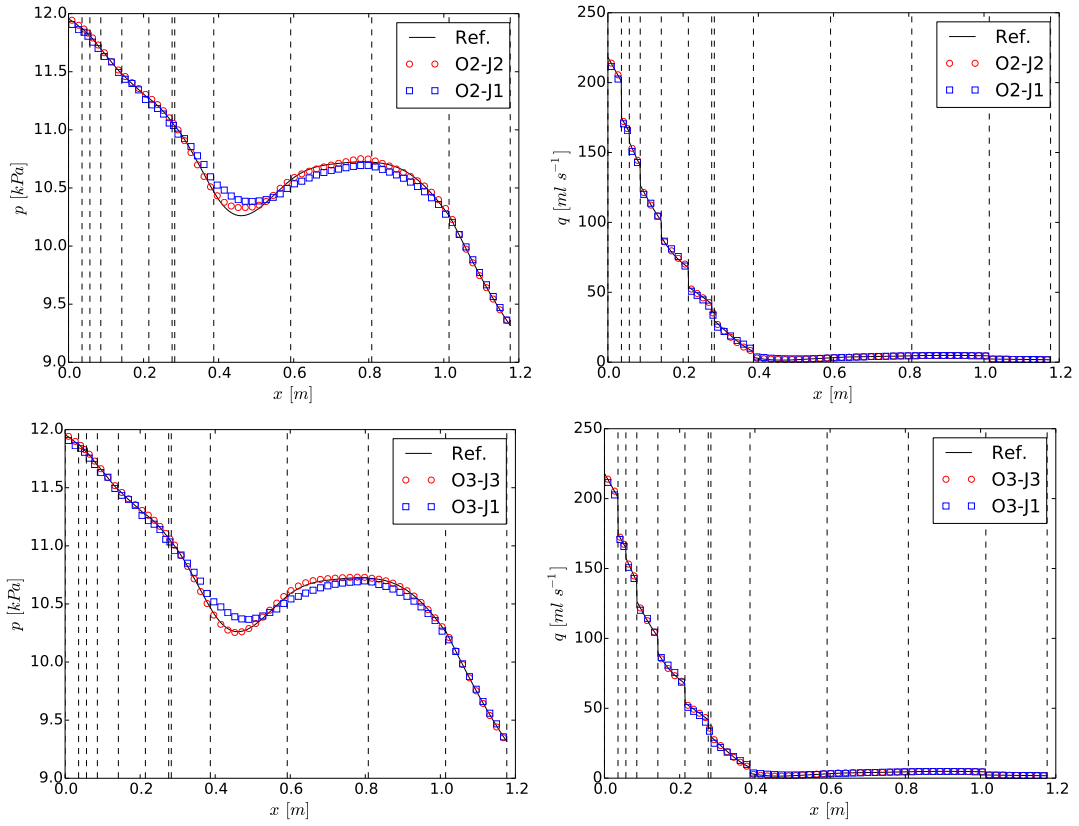
Figure 7: Second and third order computational results for pressure and flow along the aorta and lower limb at time $t = 10\,s$. Vertical lines indicate the location of bifurcations. For other quantities refer to Table 3.
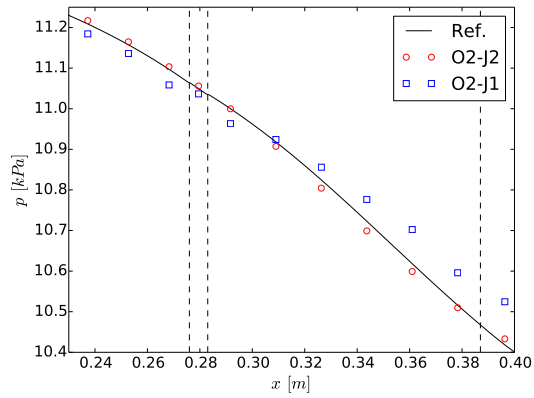

Figure 8: Detail of second order computational results for pressure along the aorta at time $t = 10\,s$. Vertical lines indicate the location of bifurcations. For other quantities refer to Table 3.

19

5. References

[1] G. Coclite, M. Garavello, B. Piccoli, Traffic flow on a road network, SIAM Journal on Mathematical Analysis 36 (6) (2005) 1862–1886. `doi:10.1137/S0036141004402683`.

[2] R. M. Colombo, M. Garavello, On the Cauchy problem for the p-system at a junction, SIAM Journal on Mathematical Analysis 39 (2008) 1456–1471.

[3] M. K. Banda, M. Herty, A. Klar, Gas flow in pipeline networks, Networks and heterogeneous media 1 (2006) 41–56.

[4] G. Leugering, J. Schmidt, On the modelling and stabilization of flows in networks of open canals, SIAM Journal on Control and Optimization 41 (1) (2002) 164–180. `doi:10.1137/S0363012900375664`.

[5] R. Borsche, A. Klar, Flooding in urban drainage systems: coupling hyperbolic conservation laws for sewer systems and surface flow, International Journal for Numerical Methods in Fluids 76 (11) (2014) 789–810. `doi:10.1002/fld.3957`.

[6] R. Colombo, M. Herty, V. Sachers, On 2×2 conservation laws at a junction, SIAM Journal on Mathematical Analysis 40 (2) (2008) 605–622. `doi:10.1137/070690298`.

[7] L. Formaggia, D. Lamponi, A. Quarteroni, One-dimensional models for blood flow in arteries, Journal of Engineering Mathematics 47 (2003) 251–276.

[8] J. Alastruey, A. W. Khir, K. S. Matthys, P. Segers, S. J. Sherwin, Pulse wave propagation in a model human arterial network: Assessment of 1-D visco-elastic simulations against *in vitro* measurements, Journal of Biomechanics 44 (2011) 2250–2258.

[9] P. J. Blanco, S. M. Watanabe, M. R. F. Passos, P. A. Lemos, R. A. Feijóo, An anatomically detailed arterial network model for one-dimensional computational hemodynamics, IEEE Transactions on Biomedical Engineering . `doi:10.1109/TBME.2014.2364522`.

[10] L. O. Müller, E. F. Toro, Well-balanced high-order solver for blood flow in networks of vessels with variable properties, International Journal for Numerical Methods in Biomedical Engineering 29 (2013) 1388–1411. `doi:10.1002/cnm.2580`.

[11] L. O. Müller, E. F. Toro, A global multiscale mathematical model for the human circulation with emphasis on the venous system, International Journal for Numerical Methods in Biomedical Engineering 30 (2014) 681–725. `doi:10.1002/cnm.2622`.

[12] M. K. Banda, M. Herty, A. Klar, Coupling conditions for gas networks governed by the isothermal euler equations, Networks and Heterogeneous Media 1 (2) (2006) 295–314. `doi:10.3934/nhm.2006.1.295`.

[13] S. J. Sherwin, L. Formaggia, J. Peiró, V. Franke, Computational modelling of 1D blood flow with variable mechanical properties and its application to the simulation of wave propagation in the human arterial system, International Journal for Numerical Methods in Fluids 43 (2003) 673–700.

[14] E. F. Toro, Riemann Solvers and Numerical Methods for Fluid Dynamics: A Practical Introduction, 3rd Edition, Springer-Verlag, Berlin Heidelberg, 2009, ISBN 978-3-540-25202-3.

[15] E. F. Toro, V. A. Titarev, Solution of the generalized Riemann problem for advection-reaction equations, Proceedings of the Royal Society A 458 (2002) 271–281.

[16] R. Borsche, J. Kall, ADER schemes and high order coupling on networks of hyperbolic conservation laws, Journal of Computational Physics 273 (2014) 658 – 670. doi:http://dx.doi.org/10.1016/j.jcp.2014.05.042.

[17] E. F. Toro, R. Millington, L. Nejad, Towards very high order Godunov schemes, in: E. F. Toro (Ed.), Godunov Methods. Theory and Applications, Vol. 1, Kluwer/Plenum Academic Publishers, New York, Boston and London, 2001, pp. 897–902, Conference in Honour of S. K. Godunov.

[18] M. Dumbser, C. Enaux, E. F. Toro, Finite volume schemes of very high order of accuracy for stiff hyperbolic balance laws, Journal of Computational Physics 227 (2008) 3971–4001.

[19] C.-W. Shu, Essentially non-oscillatory and weighted essentially non-oscillatory schemes for hyperbolic conservation laws, in: A. Quarteroni (Ed.), Advanced Numerical Approximation of Nonlinear Hyperbolic Equations, Vol. 1697 of Lecture Notes in Mathematics, Springer Berlin Heidelberg, 1998, pp. 325–432. doi:10.1007/BFb0096355.

[20] C. Hu, C. Shu, Weighted Essentially Non-oscillatory Schemes on Triangular Meshes, Journal of Computational Physics 150 (1999) 97–127.

[21] E. F. Toro, A. Siviglia, Flow in collapsible tubes with discontinuous mechanical properties: mathematical model and exact solutions, Communications in Computational Physics 13 (2) (2013) 361–385.

[22] E. E. Han, M. Hantke, G. Warnecke, Exact Riemann solutions to compressible Euler equations in ducts with discontinuous cross-section, Journal of Hyperbolic Differential Equations 9 (3) (2012) 403–449.

[23] R. Bernetti, V. A. Titarev, E. F. Toro, Exact solution of the Riemann problem for shallow water equations with discontinuous bottom geometry, Journal of Computational Physics 227 (2008) 3212–3243.

[24] P. J. Blanco, S. M. Watanabe, E. A. Dari, M. R. F. Passos, R. A. Feijóo, Blood flow distribution in an anatomically detailed arterial network model: criteria and algorithms, Biomechanics and Modeling in Mechanobiology 13 (2014) 1303–1330. doi:10.1007/s10237-014-0574-8.

[25] R. J. LeVeque, Finite volume methods for hyperbolic problems, Cambridge texts in applied mathematics, Cambridge University Press, Cambridge, New York, 2002.

[26] M. Dumbser, E. F. Toro, A Simple Extension of the Osher Riemann Solver to Non-conservative Hyperbolic Systems, Journal of Scientific Computing 48 (2011) 70–88.

[27] M. Dumbser, M. Castro, C. Parés, E. F. Toro, ADER schemes on unstructured meshes for nonconservative hyperbolic systems: Applications to geophysical flows, Computers & Fliuds 38 (2009) 1731–1748.

[28] M. Dumbser, A. Hidalgo, M. Castro, C. Parés, E. F. Toro, FORCE schemes on unstructured meshes II: Non-conservative hyperbolic systems, Computer Methods in Applied Mechanics and Engineering 199 (2010) 625–647.

[29] M. Dumbser, M. Käser, Arbitrary high order non-oscillatory finite volume schemes on unstructured meshes for linear hyperbolic systems, Journal of Computational Physics 221 (2007) 693–723.

[30] G. Jiang, C. Shu, Efficient Implementation of Weighted ENO Schemes, Journal of Computational Physics 126 (1996) 202–228.

[31] A. Hidalgo, M. Dumbser, ADER Schemes for Nonlinear Systems of Stiff Advection-Diffusion-Reaction Equations, Journal of Scientific Computing 48 (2011) 173–189.

[32] G. I. Montecinos, C. E. Castro, M. Dumbser, E. F. Toro, Comparison of solvers for the generalized Riemann problem for hyperbolic systems with source terms, Journal of Computational Physics 231 (2012) 6472–6494.

[33] C. Parés, Numerical methods for nonconservative hyperbolic systems: a theoretical framework, SIAM Journal on Numerical Analysis 44 (2006) 300–321.

[34] M. L. Muñoz Ruiz, C. Parés, On the Convergence and Well-Balanced Property of Path-Conservative Numerical Schemes for Systems of Balance Laws, Journal of Scientific Computing 48 (2011) 274–295.

[35] D. Elad, D. Katz, E. Kimmel, S. Einav, Numerical schemes for unsteady fluid flow through collapsible tubes, Journal of Biomedical Engineering 13 (1991) 10–18.

[36] B. S. Brook, T. J. Pedley, A model for time-dependent flow in (giraffe jugular) veins: uniforme tube properties, Journal of Biomechanics 35 (2002) 95–107.

[37] K. S. Matthys, J. Alastruey, J. Peiró, A. W. Khir, P. Segers, P. R. Verdonck, K. H. Parker, S. J. Sherwin, Pulse wave propagation in a model human arterial network: Assessment of 1-D numerical simulations against *in vitro* measurements, Journal of Biomechanics 40 (2007) 3476–3486.